

Optical and spectral observations and hydrodynamic modelling of Type IIb Supernova 2017gpn

Elena A. Balakina,^{1,2} Maria V. Pruzhinskaya,^{2,3*} Alexander S. Moskvitin,⁴ Sergei I. Blinnikov,^{2,3,5,6} Xiaofeng Wang,^{7,8} Danfeng Xiang,⁷ Han Lin,⁷ Liming Rui⁷, and Huijuan Wang⁹

¹ Lomonosov Moscow State University, Faculty of Physics, Leninskie Gory, 1-2, Moscow, 119991, Russia

² Lomonosov Moscow State University, Sternberg Astronomical Institute, Universitetsky pr. 13, Moscow, 119234, Russia

³ Space Research Institute, 84/32 Profsoyuznaya Street, Moscow, 117997, Russia

⁴ Special Astrophysical Observatory RAS, Nizhniy Arhyz, 369167, Russia

⁵ NRC Kurchatov institute - ITEP, B.Cheremushkinskaya 25, 117218 Moscow, Russia

⁶ Kavli IPMU, University of Tokyo, Kashiwa, 277-8583, Japan

⁷ Physics Department and Tsinghua Center for Astrophysics, Tsinghua University, Beijing, 100084, China

⁸ Beijing Planetarium, Beijing Academy of Science and Technology, Beijing, 100044, China

⁹ National Astronomical Observatory of China, Chinese Academy of Sciences, Beijing, 100012, China

Accepted XXX. Received YYY; in original form ZZZ

ABSTRACT

In this work we present the photometric and spectroscopic observations of Type IIb Supernova 2017gpn. This supernova was discovered in the error-box of LIGO/Virgo G299232 gravitational-wave event. We obtained the light curves in *B* and *R* passbands and modelled them numerically using the one-dimensional radiation hydrocode STELLA. The best-fit model has the following parameters: the pre-SN star mass and the radius are $3.5 M_{\odot}$ and $50 R_{\odot}$, respectively; the explosion energy is $E_{\text{exp}} = 1.2 \times 10^{51}$ erg; the mass of radioactive nickel is $M_{\text{Ni}^{56}} = 0.11 M_{\odot}$, which is totally mixed through the ejecta, the mass of the hydrogen envelope $0.06 M_{\odot}$. Moreover, SN 2017gpn is a confirmed SN IIb that is located at the farthest distance from the center of its host galaxy NGC 1343 (i.e. the projected distance is ~ 21 kpc). This challenges the scenario of the origin of Type IIb Supernovae from massive stars.

Key words: supernovae: general – supernovae: individual: SN 2017gpn – stars: evolution

1 INTRODUCTION

Type IIb Supernovae (SNe IIb) are characterized by spectra evolving from dominant hydrogen lines at early times to increasingly strong helium features and progressively weaker hydrogen lines later on (Filippenko et al. 1993). That is the reason why SNe IIb are regarded as an intermediate group between hydrogen-rich SNe II and hydrogen-poor SNe Ib. SNe IIb are in the class of the stripped-envelope core-collapse supernovae (CCSNe). It is supposed that progenitors of such supernovae are massive stars which have lost most of their hydrogen envelope (Clocchiatti & Wheeler 1997).

Nowadays there are two hypotheses explaining how stars can lose the hydrogen envelope. The first scenario supposes the evolution of rather massive $M \approx 25 M_{\odot}$

single star with the average mass loss rate being about $10^{-5} M_{\odot}$ per year. Such powerful stellar wind could provide required outflow of hydrogen (Hoflich et al. 1993). The second and more plausible scenario includes a mass transfer in a binary system where progenitor star is a supergiant of moderate mass (Nomoto et al. 1993; Woosley et al. 1994; Ergon et al. 2015). Massive companion expands and fills its Roche lobe, after that mass transfer starts due to the Roche lobe overflow (Yoon et al. 2017).

Nevertheless, the progenitor nature of SNe IIb is still not clear. While SNe II form a continuous group as Anderson et al. (2014) and Sanders et al. (2015) established, Pessi et al. (2019) showed that SN II light curves are distinct from those of SNe IIb with no suggestion of a continuum distribution. This fact suggests that progenitors of SNe IIb make up a separate group which is different from the SNe II ones. However, it is also could be the consequence of the lack of

* E-mail: pruzhinskaya@gmail.com

observational data: SNe IIb make up less than 5 per cent of all CCSNe according to the Open Supernova Catalog¹ (Guilochon et al. 2017) and only about 2 dozens of them have detailed multi-colour photometry appropriate for further insight study (including hydrodynamic modelling).

To extend the sample of well-studied SNe IIb, in this paper we present the photometric and spectroscopic observations of SN 2017gpn. The photometry was performed with Zeiss-1000 telescope (Komarov et al. 2020) of the Special Astrophysical Observatory of the Russian Academy of Science (SAO RAS). Spectroscopic data were obtained with the Xinglong 2.16-m telescope of the National Astronomical Observatory of China. Collected photometric data are used for the numerical light curve (LC) calculations done by the radiation hydrocode STELLA (Blinnikov et al. 1998, 2006). These simulations give us the parameters of pre-supernova star and explosion characteristics.

The interest in this supernova is also augmented by the fact that usually we observe such type of supernovae only in spiral galaxies in hydrogen-rich environment where young massive stars are being born (Filippenko 1997). In contrast to this, SN 2017gpn is located quite far from the active star formation regions and the spiral arms of the host galaxy. We also do not see any dwarf satellite galaxies at the SN location. The unusual location of SN 2017gpn in the host galaxy indicates that the existing models of SN IIb progenitors may not explain all observational data and have to be reviewed.

The paper is organized as follows. In Section 2 we describe the observations, data processing, and resulting light curves and spectra. In Section 3 we present the hydrodynamic modelling of SN 2017gpn and the parameters of the best-fit model. Section 4 contains the comparison of modelling results, LC behaviour, and spectral features of SN 2017gpn with those for other SNe IIb and the discussion of the unexpected location of SN 2017gpn relative to its host galaxy. Finally, we conclude the paper in Section 5.

2 OBSERVATIONS

2.1 Discovery

On the last day of the second Advanced Detector Observing Run “O2”, LIGO/Virgo collaboration released the G299232 alert². During the follow-up inspection of the gravitational-wave (GW) candidate error-box, on 2017 August 27.017 MASTER Global Robotic Net (Lipunov et al. 2010) discovered an optical transient named MASTER OT J033744.97+723159.0 (Lipunov et al. 2017).

On the discovery day, three spectra of MASTER OT J033744.97+723159.0 were obtained with the ACAM instrument mounted on the William Herschel Telescope on La Palma (Spain) by Jonker et al. (2017) and the analysis showed that transient classifies as SNe IIb. Further observations on 2017 August 29 obtained with the SPRAT spectrograph on the Liverpool Telescope (Copperwheat et al. 2017) and with the Xinglong 2.16-m telescope of the National Astronomical Observatory of China (Rui et al. 2017; Wang 2017) confirmed this classification by cross-correlating with

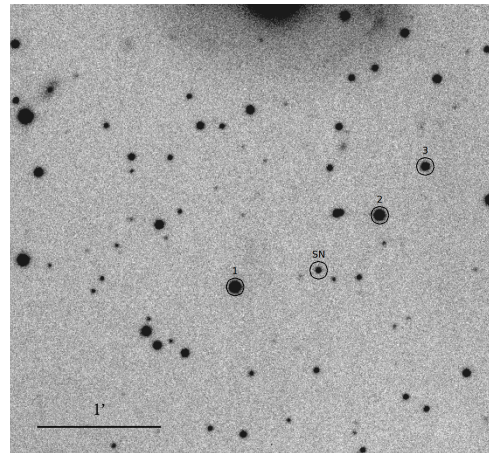


Figure 1. SN 2017gpn and comparison stars. The image is obtained with the Zeiss-1000 telescope in *R* passband.

a library of spectra with use of the Supernova Identification code (SNID; Blondin & Tonry 2007). According to SNID, the spectrum with the highest correlation coefficient belongs to Type IIb SN 1996cb at phase -2 days.

On 2017 September 6 at 03:21:12 UT, Caimmi (2017) reported the discovery of a supernova with the 0.24-m telescope from the Valdicerro Observatory. The supernova received the IAU designation AT 2017gpn and was identified as MASTER OT J033744.97+723159.0.

SN 2017gpn is located at \sim 140 arcsec from the center of the host galaxy NGC 1343 (Fig. 1). Taking into account that the redshift of NGC 1343 is 0.0073 (Springob et al. 2005) and assuming the flat Λ CDM cosmology with $\Omega_\Lambda = 0.7$ and $H_0 = 70 \text{ km s}^{-1} \text{ Mpc}^{-1}$, we obtain that the projected distance between SN 2017gpn and the center of its host is \sim 21 kpc.

2.2 Photometric data processing

We performed 20 epochs of observations (*B* and *R* passbands) with CCD-photometer on the Zeiss-1000 telescope of SAO RAS. The aperture photometry was performed using standard procedures of ESO-MIDAS software package. It includes standard image processing such as bias subtraction and flat field correction, removing the traces of cosmic particles, and stacking of individual frames into the summary image.

Since no Landolt or any other standards (Landolt 1992; Stetson 1987) were available for this region, we use the Pan-STARRS (Chambers et al. 2016; Flewelling et al. 2016) magnitudes for comparison stars. These magnitudes were recalculated from *g*, *r*, *i* passbands to *B* and *R* with the use of Lupton’s transformation equations³:

$$\begin{aligned} B &= g + 0.3130(g - r) + 0.2271, & \sigma &= 0.0107 \\ R &= r - 0.1837(g - r) - 0.0971, & \sigma &= 0.0106 \\ R &= r - 0.2936(r - i) - 0.1439, & \sigma &= 0.0072 \end{aligned} \quad (1)$$

The comparison stars are shown in Fig. 1 and their magnitudes are listed in Table 1.

¹ <https://sne.space>

² <https://gcn.gsfc.nasa.gov/other/G299232.gcn3>

³ <http://www.sdss3.org/dr8/algorithms/sdssUBVRITransform.php>

Table 1. Magnitudes of the comparison stars in B and R passbands derived from g , r , i Pan-STARRS1 magnitudes using Lupton's 2005 transformation equations.

Nº	B	err $_B$	R	err $_R$
1	16.447	0.011	15.032	0.015
2	16.859	0.012	15.428	0.015
3	17.705	0.011	16.636	0.017

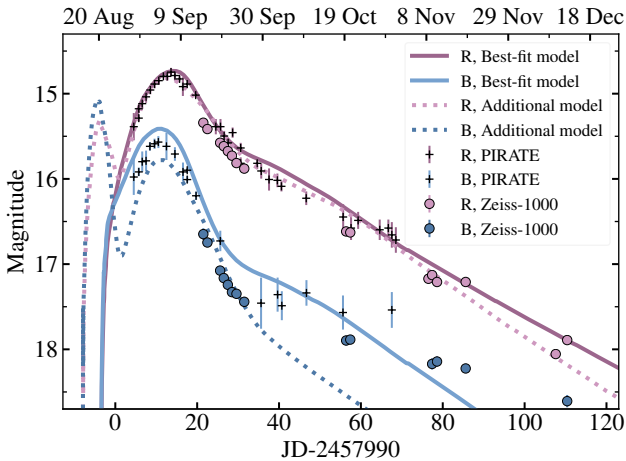


Figure 2. Light curve of SN 2017gpn. Pink and blue solid lines correspond to the best-fit model, dashed lines — to the additional model in R and B passbands, respectively. Circles are the Zeiss-1000 data, crosses are the data taken from [Roberts & Kolb 2018](#).

The line-of-sight reddening in our galaxy is adopted to be $E(B - V) = 0.30$ mag ([Schlafly & Finkbeiner 2011](#)) that corresponds to the additive magnitude correction of 1.246 and 0.725 mags for B and R passbands, respectively. Since SN 2017gpn is very far from the center of NGC 1343, we assume that the host's contamination is negligible. Resulting photometric data are presented in Table 2.

2.3 Resulting light curves

With Zeiss-1000 observations we can restore only the post-maximum part of the light curve. That is why to improve the accuracy of the further hydrodynamic modelling (see Section 3) we supplemented our data with observations in B and R passbands from [Roberts & Kolb 2018](#) obtained with the PIRATE robotic telescope in Spain ([Holmes et al. 2011](#)). The resulting light curve is presented in Fig. 2. The data points obtained at Zeiss-1000 (shown as circles) and the data points taken from [Roberts & Kolb 2018](#) (marked with crosses) mutually complement each other and allow us to restore B and R light curves almost entirely.

One can notice a slight shift between two data sets. This may be due to the different source of photometry for the comparison stars since there are no Stetson and Landolt photometric standards in this field. However, the difference between the values is less than the uncertainty associated with the choice of hydrodynamic model, therefore for our purpose it can be neglected.

Table 2. Photometric observations of SN 2017gpn with the Zeiss-1000 telescope. The magnitudes are corrected for the expected Galactic foreground extinction.

JD 2457990+	B	err $_B$	R	err $_R$
21.5	16.65	0.07	15.34	0.03
22.5	16.75	0.05	15.41	0.02
25.6	17.08	0.05	15.58	0.03
26.5	17.16	0.05	15.62	0.04
27.5	17.24	0.06	15.67	0.02
28.5	17.33	0.06	15.73	0.02
29.6	17.35	0.05	15.81	0.02
31.5	17.44	0.06	15.88	0.03
56.4	17.90	0.06	16.62	0.02
57.4	17.89	0.05	16.63	0.01
76.5	—	—	17.17	0.03
77.4	18.17	0.07	17.13	0.03
78.6	18.14	0.06	17.21	0.03
85.6	18.22	0.05	17.21	0.03
107.6	—	—	18.06	0.04
110.4	18.61	0.07	17.89	0.03
143.3	19.14	0.15	18.78	0.01
153.3	—	—	18.54	0.30
224.3	—	—	21.14	0.20

2.4 Spectra

The spectroscopic observations were collected using the Xinlong 2.16-m telescope and the BFOSC system. All the spectra were reduced using routine tasks within IRAF and the flux was calibrated with spectrophotometric standard stars observed on the same nights. Telluric lines are removed from all of these spectra. The journal of our spectroscopic observations is given in Table 3.

Three optical spectra were obtained for SN 2017gpn, covering the phases from -8.3 days to $+19.7$ days from the R -band maximum light (peak time is JD = 2458003.6), which are shown in Fig. 3. At one week before the peak, the spectrum shows strong Balmer lines of hydrogen, providing evidence of a Type II Supernova. Moreover, the existing prominent absorption features at ~ 5670 and 6860 Å that can be identified as $\text{He I } \lambda 5876$ and $\text{He I } \lambda 7065$, respectively, confirming that SN 2017gpn can be further put into the Type I Ib subclass. From the absorption minima of $\text{H} \alpha$ and $\text{He I } \lambda 5876$ lines at the first obtained spectrum, we measured the ejecta velocity as 15000 ± 130 and 10100 ± 300 km s $^{-1}$, respectively, indicating that the Balmer lines and the He I lines originated from different layers (see Table 3). At two weeks after the maximum, the helium features seem to become more noticeable and other helium features such as $\text{He I } \lambda 6678$ (blueshifted to ~ 6510 Å) emerge in the spectrum. The helium features become even more pronounced in the spectrum taken one week later, while the hydrogen features become gradually weak. The overall spectral evolution of SN 2017gpn is presented in Fig. 3 and it is similar to other typical Type I Ib Supernovae, like SN 1993J ([Barbon et al. 1995](#)), SN 1996cb ([Qiu et al. 1999](#)), and SN 2008ax ([Modjaz et al. 2014](#)).

Table 3. Journal of spectroscopic observations of SN 2017gpn with the BFOSC+G4 instrument of the Xinglong 2.16-m telescope. Values of the ejecta velocity measured from the absorption lines of H α , He I $\lambda 5876$, Fe II $\lambda 5018$, and Fe II $\lambda 5169$ are also presented.

JD 2457990+	Exp. Time [s]	H α [km s $^{-1}$]	He I $\lambda 5876$ [km s $^{-1}$]	Fe II $\lambda 5018$ [km s $^{-1}$]	Fe II $\lambda 5169$ [km s $^{-1}$]
5.30	3600	15000 ± 130	10100 ± 300	12000 ± 1200	11400 ± 950
25.29	3600	13200 ± 100	8000 ± 100	6750 ± 470	5130 ± 490
33.33	2700	12900 ± 200	7300 ± 200	—	—

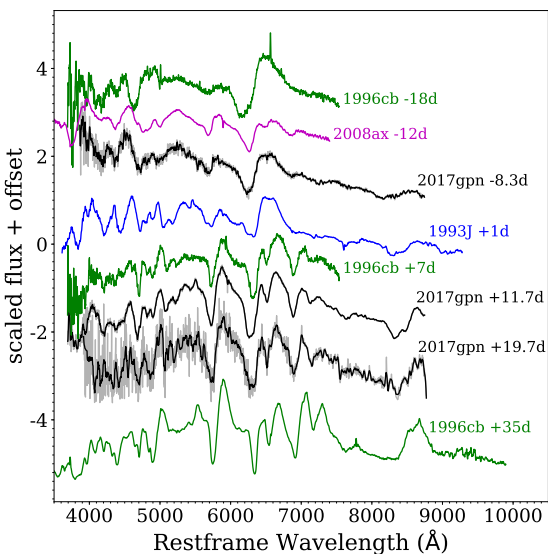


Figure 3. Three spectra of SN 2017gpn at different phases, the observation dates are indicated with respect to the R -band maximum light at JD = 2458003.6. Spectra of SNe IIb 1993J, 1996cb, and 2008ax are presented for comparison.

3 MODELLING

3.1 Pre-supernova models

A set of non-evolutionary pre-supernova models is obtained under the assumption of a power-law dependence of temperature on density: $T \propto \rho^\alpha$ (Nadyozhin & Razinkova 1986; Blinnikov & Bartunov 1993). Therefore, the obtained hydrostatic configuration would be close to a polytrope of index $1/\alpha \approx 3$. The deviation from the polytropic model increases in the outer layers due to recombination of ions and non-homogeneous chemical composition.

At the center of such configuration we isolated a point-like source of gravity that has a non-negligible influence on the expansion of the innermost layers of supernova ejecta. Mass and radius of this compact remnant is adopted to be $M_{\text{CR}} = 1.41 M_\odot$ and $0.01 R_\odot$ for all treated pre-SN models.

In our approach we do not follow the explosive nucleosynthesis. Thus, the SN ejecta composition is the same as the pre-SN composition except for ^{56}Ni . Since the amount and distribution of ^{56}Ni synthesized during the explosion plays a crucial role in the SN luminosity evolution, we consider two radial distribution for ^{56}Ni . In the first one ^{56}Ni is

totally mixed trough the ejecta and in the second one ^{56}Ni falls off from the center.

As input parameters for the further hydrodynamical modelling, we varied the pre-SN star mass M and the radius R , the mass of synthesized nickel $M_{^{56}\text{Ni}}$, and the initial distribution of chemical elements in the pre-SN star.

3.2 STELLA code

To explode the hydrostatic non-evolutionary pre-SN models a one-dimensional multi-frequency radiation hydrocode STELLA is used. The full description of the code can be found in Blinnikov et al. (1998, 2006); a public version of STELLA is also included with the MESA distribution (Paxton et al. 2018). The STELLA code is used for the light curve modelling of different types of SNe — Ia (Blinnikov et al. 2006), Ib/Ic (Folatelli et al. 2006; Tauris et al. 2013), IIb (Blinnikov et al. 1998; Tsvetkov et al. 2012), IIn (Chugai et al. 2004), IIP (Baklanov et al. 2005; Tominaga et al. 2009), Ic associated with long gamma-ray bursts (Volnova et al. 2017). The STELLA code was compared with the other well-known hydrodynamic codes and found to be in a good agreement with them on the level of several per cent (e.g. Woosley et al. 2007; Kromer & Sim 2009; Sim et al. 2010; Kozyreva et al. 2017; Tsang et al. 2020).

In the current calculations, we adopted 100 zones for the Lagrangian coordinate and 130 frequency bins. The explosion is initiated by putting thermal energy into the innermost layers. The energy released in 0.1 sec, that is less than the hydrodynamic time of the pre-supernova. While this condition is true, the resulting light curve is not affected by the details of explosion mechanism (Imshennik & Nadezhin 1983).

3.3 Best-fit model

To determine the best-fit model of SN 2017gpn we consider a grid of parameters. The pre-SN mass varies between $3.5 M_\odot$ and $5.5 M_\odot$ with a step of $0.5 M_\odot$; the pre-SN radius and E_{exp} takes the values $\{50, 100, 200, 400, 600\} R_\odot$ and $\{0.6, 1.2, 2.4\} \times 10^{51}$ erg, respectively; three different $M_{^{56}\text{Ni}}$ $\{0.07, 0.09, 0.11\} M_\odot$ are considered, both with and without mixing. The mass of hydrogen envelope $M_{\text{H,env}}$ is adopted to be $0.06 M_\odot$ which is in line with our expectations for Type IIb Supernovae.

After determination of parameter grid we built trial models and chose the best-fit model within the generated grids of light curves by calculating χ^2 in R passband. The best-fit model corresponds to the minimum value of χ^2 . We do not provide any statistical uncertainties, since this procedure requires enormous computational efforts. Instead,

Table 4. Parameters for the best-fit and the additional hydrodynamic models of SN 2017gpn.

Parameter	Best-fit model	Additional model
R	$50 R_\odot$	$400 R_\odot$
M	$3.5 M_\odot$	$3.5 M_\odot$
$M_{\text{H_env}}$	$0.06 M_\odot$	$0.21 M_\odot$
M_{CR}	$1.41 M_\odot$	$1.41 M_\odot$
$M_{^{56}\text{Ni}}$	$0.11 M_\odot$, mixed	$0.11 M_\odot$, no mixing
E_{exp}	1.2×10^{51} erg	1.2×10^{51} erg
$t_{\text{peak}, R}$	7.5 Sep 2017	5.6 Sep 2017

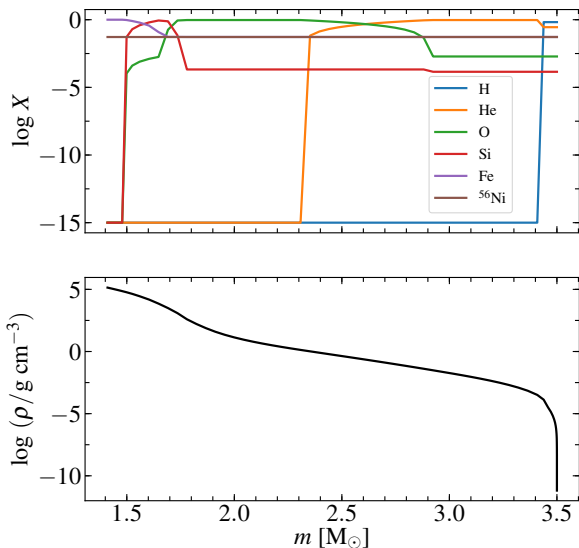


Figure 4. Mass fractions of the most abundant chemical elements in the ejecta (top) and density profile (bottom) for the best-fit pre-SN star model with respect to the interior mass. The central region of $1.41 M_\odot$ is taken away.

optimal model is recovered as a compromise between the fits to the observed light curve and the evolution of the velocity at the photosphere (see Section 4.2.1). The values of the best-fit model parameters are summarized in Table 4. Fig. 2 compares the light curves of the model (solid lines) with the observations of SN 2017gpn.

In Fig. 4 we also show the distribution of the chemical elements and the density profile for a pre-SN star. Note that the best-fit model shows a small amount of hydrogen in the pre-SN star composition, which is expected for SNe IIb (Filippenko et al. 1993). ^{56}Ni is totally mixed through the ejecta.

3.4 The influence of the model parameters on the light curve

To provide a reasonable range of the best-fit model parameters, we consider the dependence of the numerical LCs on an input parameter of the model while the others remain fixed. We vary the mass M and the radius R of the pre-

SN star, the mass of synthesized ^{56}Ni and the energy of the explosion E_{exp} . In Fig. 5 we plot some modelled LCs in R passband which show a valid range for each parameter. All presented models are slightly shifted along the time axis to better describe the observational light curve.

The first considered parameter is the pre-SN mass M, see Fig. 5 (a). This parameter mainly affects the width of the light curve so that the light curve becomes broader with the mass increase. It explains by the fact that having a small mass the envelope becomes transparent faster. Thus, the LC increases before the maximum light and decreases rapidly after it. As Fig. 5 (a) shows, the range of valid pre-SN mass is $3\text{--}4 M_\odot$.

The next parameter is the amount of synthesized ^{56}Ni (Fig. 5 (b)). The models are brighter for higher ^{56}Ni mass. The LCs corresponding to the ^{56}Ni mass of $0.09 M_\odot$ and $0.13 M_\odot$ lie below and above the best-fit model light curve, respectively. These two values define the acceptance range of $M_{^{56}\text{Ni}}$ model parameter.

The pre-SN radius affects mainly the light curve tail: the larger radius value corresponds to the brighter light curve after maximum light. The chosen range of the pre-SN radius is $20\text{--}70 R_\odot$, see Fig. 5 (c).

The last parameter we vary is the explosion energy E_{exp} , see Fig. 5 (d). The determined range for the energy parameter is $(1.05\text{--}1.60) \times 10^{51}$ erg. As it follows from Fig. 5 (d), the smaller values of E_{exp} correspond to the brighter light curves. This dependence is in line with our expectations. The larger E_{exp} , for fixed mass of ^{56}Ni and fixed total mass, implies higher velocities, hence, less trapping of gamma-ray photons. This leads to the increase of the predicted observed gamma-ray flux and, therefore, to the decrease of the emission in the visible light range.

4 DISCUSSION

4.1 Comparison with other SNe IIb

We collected data for well-studied SNe IIb with a good photometric coverage in B and R passbands, for which results of hydrodynamic modelling can be found in the literature. In Fig. 6 the light curves of chosen SNe IIb are presented. It could be noticed that LCs in B and R passbands are similar — characteristic bell-shaped LCs. Moreover, as Pessi et al. (2019) showed, SNe IIb take longer to reach maximum light and decline more quickly post maximum than hydrogen-rich SNe II, so authors assume there is no continuum between SNe IIb and other SNe II like between SNe IIP and IIL types. SN 2017gpn has a typical SN IIb light curve, and belongs to one of the brightest well-studied SNe IIb: it is brighter than a typical member of Type IIb SN 1993J by 0.75 mag in R passband.

4.1.1 Classification of Prentice & Mazzali (2017)

Following Prentice & Mazzali (2017), stripped-envelope SNe should be sub-classified into four groups: Ib, Ib(II), IIb, and IIb(I), using the additional parameters — equivalent width of H α ($EW_{\text{H } \alpha}$) and H α emission to absorption ratio $f_{\text{em}}/f_{\text{abs}}$. $EW_{\text{H } \alpha}$ parameter value is $> 60\text{\AA}$ for supernovae of IIb(I) group, $20 < EW_{\text{H } \alpha} < 60\text{\AA}$ for Ib(II), and takes any

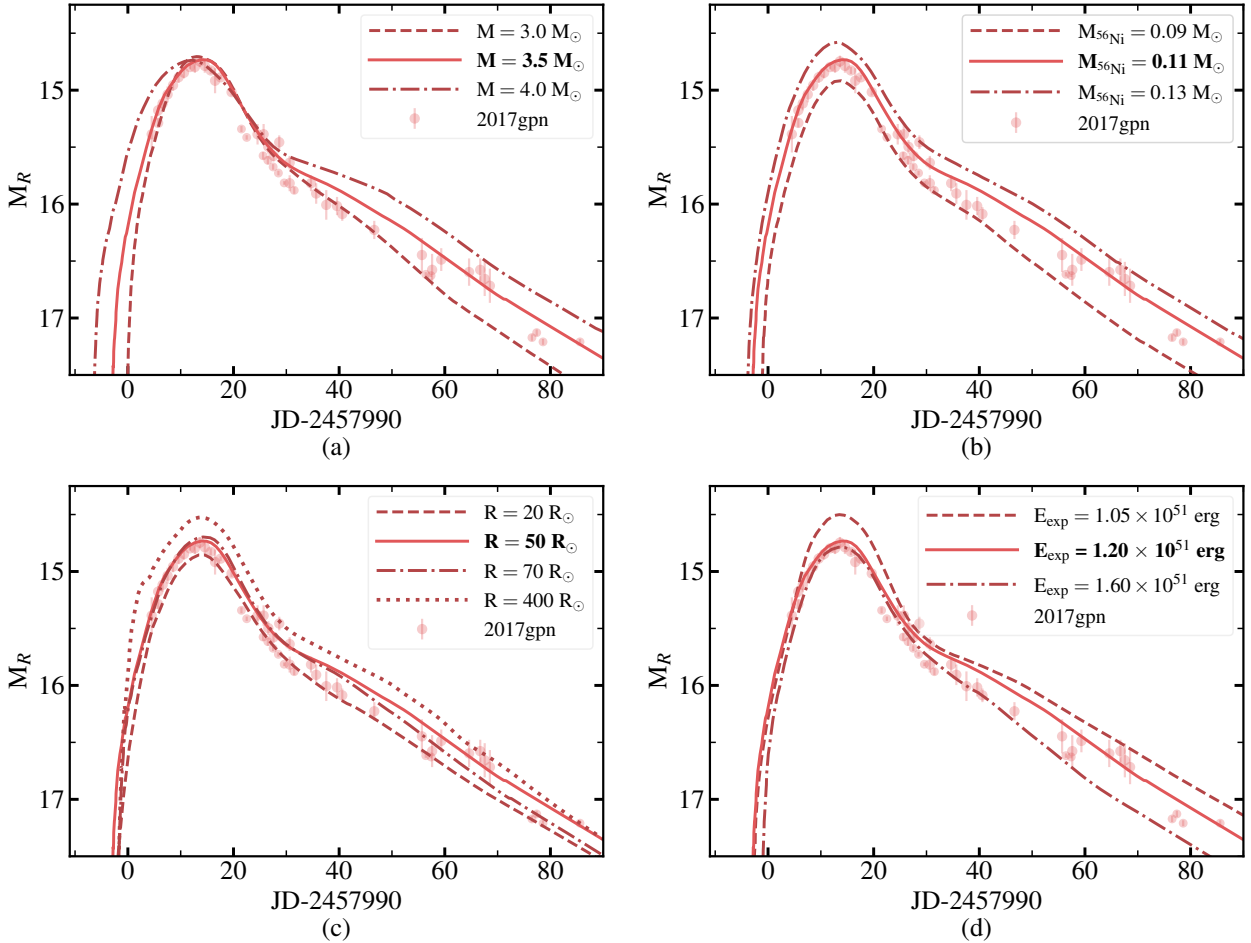


Figure 5. The dependence of the modelled R -passband LC on the pre-SN mass M (a), the amount of synthesized ^{56}Ni (b), the pre-SN radius R (c), and the explosion energy E_{exp} (d). All models are shifted along the time axis to better describe the observations. Best-fit model is shown with solid line in all plots, observations are shown with circles.

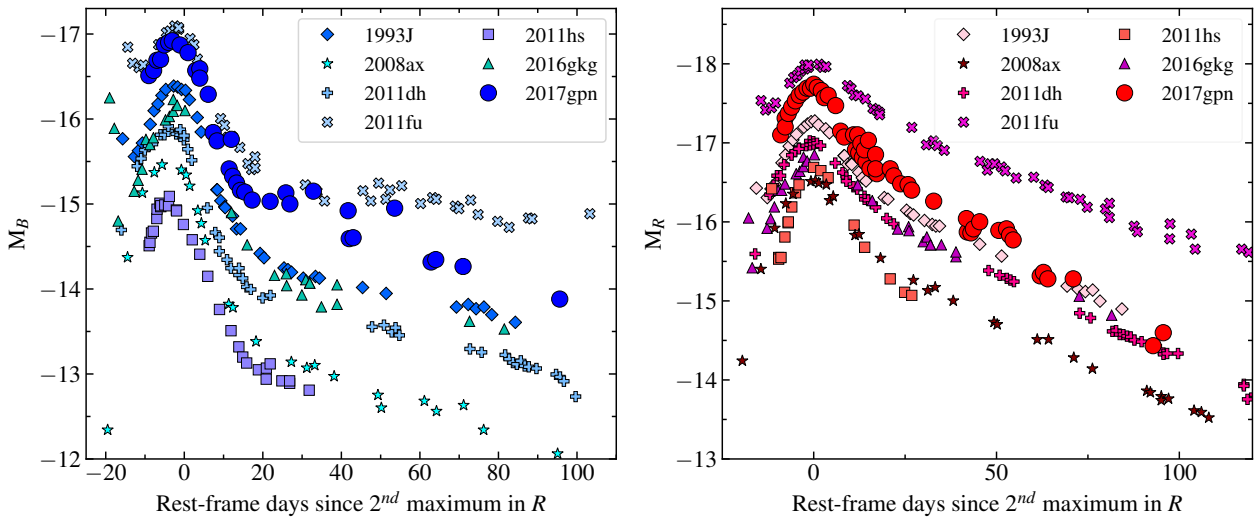


Figure 6. M_B and M_R light curves of SN 2017gpn in comparison with those of other Type I Ib/S supernovae: 1993J (Richmond et al. 1996), 2008ax (Tsvetkov et al. 2009), 2011dh (Tsvetkov et al. 2012), 2011fu (Kumar et al. 2013), 2011hs (Bufano et al. 2014), 2016gkg (Bersten et al. 2018).

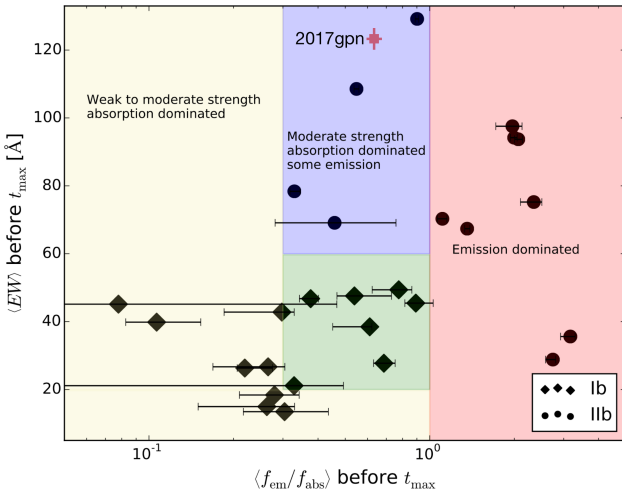


Figure 7. The figure is borrowed from Prentice & Mazzali 2017 (figure 7) with plotted SN 2017gpn (pink square). It illustrates the stripped-envelope supernovae sub-classification based on the comparison of the line strength (equivalent width of H α) against the line profile (H α emission to absorption ratio f_{em}/f_{abs}) as proposed by Prentice & Mazzali (2017). SN 2017gpn lies in the blue region which corresponds to IIb(I) group. Groups IIb, Ib and Ib(II) are in red, yellow and green regions, respectively.

reasonable values for Ib and IIb groups. The H α emission to absorption ratio f_{em}/f_{abs} differs for IIb and IIb(I) groups: it ranges from 0.3 to 1 for IIb(I) and it is greater than 1 for IIb group (see Fig. 7).

We calculated the intensity and equivalent width of H α in our first spectrum (-8.3 days before R -band maximum) for SN 2017gpn and found $f_{em}/f_{abs} = 0.63 \pm 0.04$, $EW_{H\alpha} = 123 \pm 3$ Å. Therefore, SN 2017gpn belongs to IIb(I) group which means it might have less hydrogen in the envelope than those most H-rich SNe such as 1993J, 2011fu, or 2011dh (see Table 5). However, it is similar to other SNe IIb(I) — 2008ax and 1996cb (the first position in a cross-correlation list according to SNID).

4.1.2 Hydrodynamic models of other SNe IIb

We compare the results of numerical simulations for SN 2017gpn and other SNe IIb (incl. IIb and IIb(I) groups of Prentice & Mazzali 2017) presented in Fig. 6. Only hydrodynamic modelling of supernovae are chosen for comparison, we do not consider any analytical light-curve modelling or scaling to templates. The modelling results are summarised in Table 5, where M_{CR} is the mass of a compact object (generally this is a neutron star) and M_{ej} is the mass of ejected matter.

The main modelling parameters such as the ejecta mass M_{ej} , the mass of ^{56}Ni , M_{H_env} , the explosion energy E_{exp} are consistent with each other. An exception is the parameter of the pre-supernova radius R . The considered hydrodynamic modelling shows that pre-SN radius lies in a broad range from 30 to $720 R_\odot$ and may be different for the same object in different models. For example, there are two models for SN 2008ax, one with a radius of $30\text{--}50 R_\odot$ (Folatelli et al. 2015) and another one with $R = 600 R_\odot$ (Tsvetkov et al.

2009). It should be noted that SN 2008ax belongs to the same group of IIb(I) supernovae as SN 2017gpn.

4.2 Additional model

Motivated by the discrepancy in modelled radius for different SNe IIb, we have found another physically reasonable model for SN 2017gpn with $R = 400 R_\odot$. For this additional model, radioactive nickel is located in the central part of the ejecta. We have also increased the mass of the hydrogen envelope to $0.21 M_\odot$, which is consistent with the fact that more extended SNe IIb should be also more H-rich (Prentice & Mazzali 2017). The parameters of the additional model are listed in Table 4. This model also well describes the observational data and agrees with the results of the hydrodynamic simulations for other SNe IIb.

There is no direct method to solve the inverse problem, i.e. to determine the parameters of the pre-supernova from the observational data. We can only build a model with given parameters and see how accurately it fits the data. Sometimes it can happen that models with different parameters reproduce observations equally well, as we see for our best-fit and additional models (Fig. 2). However, if some additional information is available, e.g. observational photospheric velocities, we can compare our theoretical estimations with the observational values and make a choice between the models.

4.2.1 Photospheric velocities

Based on three spectra of SN 2017gpn obtained at different epochs with the Xinglong 2.16-m telescope, we measured the ejecta velocity from H α and He I $\lambda 5876$ absorption lines (Table 3). In Fig. 8 we show the comparison between the velocities measured from these lines and theoretical values from the STELLA code, which are the velocities of photosphere at $\tau = 2/3$ level. The best-fit model is consistent with the velocity measured from H α line for this epoch, the additional model is in good agreement with He I $\lambda 5876$ velocities for all three epochs.

It should be noted that P-Cygni profiles are formed in all layers above the photosphere. Hence, the hydrogen and helium features do not necessarily reflect the photospheric velocities calculated by our hydrodynamic modelling. It has to be taken into account that the growth of the Sobolev optical depth (Sobolev 1960) at the photosphere level causes a significant blueshift of the P-Cygni profile minimum, so the resulting velocity in that case will be overestimated (Kasen et al. 2002). This effect may explain why the velocities measured from H α line are greater than our theoretical estimations in Fig. 8. Meanwhile, according to Dessart & Hillier (2005, 2006) the velocities measured from strong lines can be both smaller and larger than the photospheric ones.

Therefore, it is more reasonable to use “weak” lines, i.e. lines with the small Sobolev optical depth, to estimate v_{ph} . Dessart & Hillier 2005 show that Na I D, Fe II $\lambda 5018$, Fe II $\lambda 5169$ are the most suitable lines to measure the photospheric velocities. We measured the velocities from Fe II $\lambda 5018$ and Fe II $\lambda 5169$ lines for the first and second epochs of observations, the last epoch spectrum has a low signal-to-noise ratio to perform the measurements. We could not determine the velocities using Na I D features since they are close to He I $\lambda 5876$ line, which is quite strong in SNe IIb.

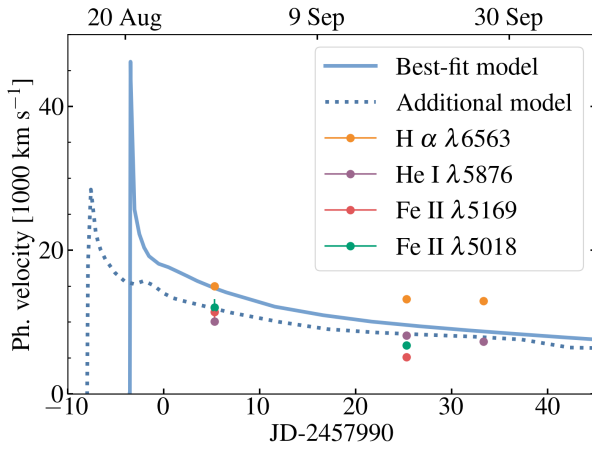


Figure 8. Photospheric velocity at $\tau = 2/3$ level as a function of time for the best-fit model (solid line) and for the additional model of higher radius (dashed line); dots are the observational velocities measured from $H\alpha$, $HeI\lambda 5876$, $FeII\lambda 5018$, and $FeII\lambda 5169$ absorption lines.

The photospheric velocities derived for the additional model slightly better correspond to the velocities from $FeII\lambda 5018$ and $FeII\lambda 5169$ lines for the first epoch of observations. For the second epoch the measured velocities are lower than STELLA values for both models. Taking into account the modelling uncertainties it is difficult to choose between the models based on these measurements only.

4.2.2 ^{56}Ni mixing

From the theoretical bolometric LCs (Fig. 9) as well as LCs in filters (Fig. 2) it can be noticed that the light curve corresponding to the model with the uniform distribution of nickel behaves differently from the light curve which conforms with the model where nickel is concentrated in the center of ejecta. This is due to the fact that in the former case the radioactive decay energy contributes to the overall energy immediately after the explosion. Whereas in the latter case we observe two peaks at the light curve. The primary peak is associated with the heating of the outer layers of the star by the shock wave which is created by the rebound of the freely falling inner layers from the collapsed core. After that the envelope expands, cools, and therefore becomes transparent. The second peak is associated with the luminescence of the inner layers heated by the radioactive decays of ^{56}Ni and its products. For the additional model we fit the observed LCs by the second peak. Due to that the best-fit and additional models are shifted relative to each other in Fig. 2. The influence of ^{56}Ni mixing on the LCs behaviour is seen as well if we compare the additional model with the model in Fig 5 (c) (dotted line) with $R = 400 R_\odot$ and ^{56}Ni totally mixed through the ejecta. Unlike the additional model, this model does not describe the observations anymore.

In Fig. 9 we also show the bolometric light curve of SN 2017gpn restored from the available photometry. To construct the bolometric light curve the SUPERBOL code is used (Nicholl 2018). To account for flux that is not covered by the observations, the black body extrapolation is applied.

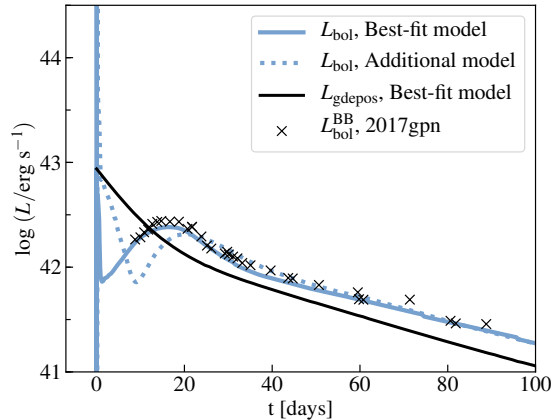


Figure 9. Theoretical bolometric light curves for the best-fit (blue solid line) and for the additional model (blue dashed line) of SN2017gpn. The crosses show the bolometric luminosity of SN 2017gpn calculated from B and R light curves with use of the SUPERBOL code (Nicholl 2018). The shift between the data and the best-fit model is the same as in Fig. 2 but transformed to the rest frame. Black solid line is the power due to the gamma-ray deposition from ^{56}Ni and ^{56}Co decays for our best-fit model. With account for the light travel time correction, L_{gdepos} satisfies the Arnett's law — going through the maximum of L_{bol} .

Even though we use only two passbands (B and R) the obtained bolometric LC agrees very well with our theoretical estimations.

4.3 Arnett's law

Arnett's law (Arnett 1982) states that the energy released on the surface at maximum light is equal to the energy deposited by gamma-ray radiation. This law is commonly used to estimate the amount of nickel produced in the explosion when the total luminosity at peak is known (Branch 1992). We plot the theoretical bolometric light curve and the curve corresponding to gamma-ray deposition from ^{56}Ni and ^{56}Co decays for our best-fit model to check this law. As we can see from Fig. 9, the law is quite well satisfied, however, the power from gamma-ray deposition does not directly go through the L_{bol} peak. This is explained by the fact that the Arnett's law is not exact and in particular assumes the infinite speed of light. In STELLA code the energy released in the center will be “seen” with a delay of R/c , where R is the radius of the expanding ejecta that changes with time and c is the speed of light. The observed difference increases towards the tail since the radius increases as well.

4.4 SN 2017gpn position relative to the host galaxy center

Supernova 2017gpn exploded in the spiral galaxy NGC 1343 at the projected distance $D \approx 21$ kpc from its center (see Fig. 1). Such location is unusual for core-collapse supernovae, in particular for Type IIb, since it is believed that stripped-envelope CCSNe are formed from very massive stars in star formation regions of galaxies (see Audcent-Ross et al. 2019 and references therein). Assuming that

Table 5. Comparison of the hydrodynamic modelling results for different SNe IIb.

SN name	M_{CR} [M_{\odot}]	M_{ej} [M_{\odot}]	M_{56Ni} [M_{\odot}]	$M_{\text{H_env}}$ [M_{\odot}]	R [R_{\odot}]	E_{exp} [10^{51} erg]	Reference
1993J	~1.4	1.4–3.1	0.06–0.08	0.2	430–720	1.2	Woosley et al. (1994) Blinnikov et al. (1998)
2008ax	1.41	2.39	0.11	—	600	1.5	Tsvetkov et al. (2009)
2008ax	1.5	1.8–3.5	0.05–0.07	0.06	30–50	0.8–1.2	Folatelli et al. (2015)
2011hs	1.5	1.5–2.5	0.04	<0.5	500–600	0.85	Bufano et al. (2014)
2011fu	1.5	3.5	0.15	0.3	450	1.3	Morales-Garoffolo et al. (2015)
2011dh	1.41	2.24–4.24	0.07	—	150–300	2–4	Tsvetkov et al. (2012)
2011dh	1.5	2	0.06	0.1	200	0.6–1	Bersten et al. (2012)
2011dh	1.5	1.56	0.075	0.1	200–300	0.58	Ergon et al. (2015)
2016gkg	1.4	3.55	0.2	0.02	180–260	1.3	Piro et al. (2017)
2016gkg	1.5–1.6	2.5–3.4	0.085–0.087	0.01–0.09	300–340	1–1.2	Bersten et al. (2018)

SN 2017gpn belongs to the galactic disk we can take into account the projection effect. The deprojected distance D_{dep} between the supernova and the host center is calculated as

$$D_{\text{dep}} = D \sqrt{\cos^2 \alpha + \sin^2 \alpha \sec^2 i}, \quad (2)$$

where α is the angle between the projected distance and the major axis of a galaxy, i is the disk inclination angle. According to HyperLeda i equals 67.3 deg and the major axis position angle of NGC 1343 is 78.8 deg (Makarov et al. 2014). Using these values and the coordinates of SN 2017gpn and its host galaxy center we can calculate the deprojected distance for SN 2017gpn, which is ~52 kpc. To understand how exceptional this position is we study the absolute and relative separations between the supernova positions and their host galaxy centers for a sample of SNe IIb.

Hereafter, by the distance between a supernova and its host galaxy we mean the projection of the distance onto the picture plane, which is obviously smaller than the real distance. However, the star evolution theory predicts that CCSNe including SNe IIb mainly appear into the galactic plane of spiral galaxies, in the regions of the high star formation rate. Therefore, we assume that the contribution of the projection onto the line of sight is relatively small and this underestimation of the distance could not significantly affect our analysis.

We collected 71 confirmed SNe IIb and 108 candidates to SNe IIb from the Open Supernova Catalog (Guillochon et al. 2017). The confirmed SNe IIb are supernovae for which the multiple spectra have been obtained and the detailed spectral analysis has been performed. If only a spectrum is available (usually single spectroscopic confirmation following the astronomical telegram about the transient discovery) we consider a supernova as a SN IIb candidate.

First, we calculated the absolute galactocentric distance D for each object as $D \approx d_a \times \Theta$. The angle Θ — angle between supernova and the host galaxy center. The angular distance d_a for the flat Λ CDM cosmology with $\Omega_{\Lambda} = 0.7$ and $H_0 = 70 \text{ km s}^{-1} \text{ Mpc}^{-1}$ is

$$d_a = \frac{c}{H_0 \times (1+z)} \int_0^z \frac{dz'}{\sqrt{(1-\Omega_{\Lambda}) \times (1+z')^3 + \Omega_{\Lambda}}}, \quad (3)$$

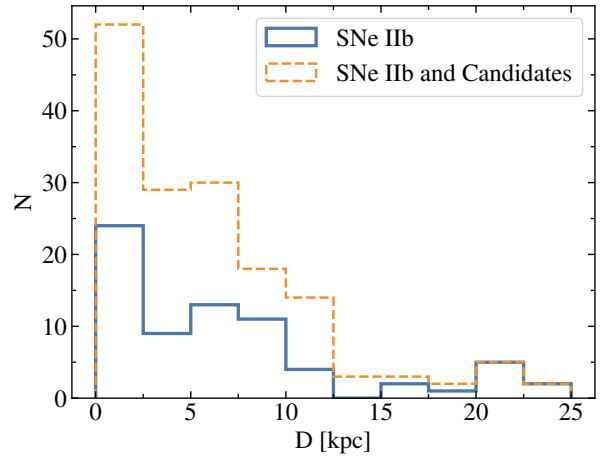


Figure 10. Histogram of the supernovae distribution depending on the projection of the distance between SN and its host galaxy center, D . Orange dashed line corresponds to all considered supernovae including confirmed SNe IIb and candidates to SNe IIb. Solid blue line corresponds to the distribution of only confirmed SNe IIb.

where z is the redshift, c is the speed of light. The distribution of Type IIb Supernovae by D is presented in Fig. 10. Most of SNe IIb, about 85 per cent, are located inside the radius of 12 kpc. However, there is a local maximum near 20 kpc value which may be due to the fact that the radius of galaxies can vary widely.

To perform a more accurate analysis we determined the SN-host separation relative to the host size. To characterise the size of a galaxy we used a D_{25} value, which is the major diameter measured to B passband 25 mag arcsec $^{-2}$ isophote. The D_{25} values were extracted from the HyperLeda extragalactic database (Makarov et al. 2014).

The full list of studied supernovae as well as the absolute and relative distances are summarised in Table A1: the first column is the number in the list for easier search, the second column consists of the supernova names starting with confirmed SNe IIb, and continued below with SNe IIb

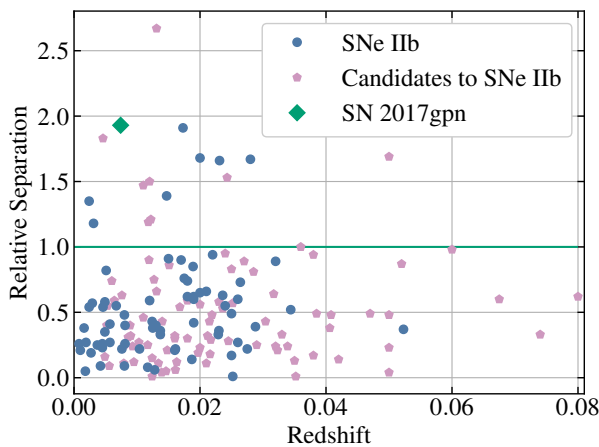


Figure 11. Relative separation between supernovae and their host galaxy centers as a function of redshift. Confirmed SNe IIb are plotted in blue dots, candidates to SNe IIb — in pink pentagons, studied SN 2017gpn is marked with the green diamond. SNe above the green line are considered to be distant from the centers of their hosts.

candidates. The equatorial coordinates (R.A, DEC.) of supernovae and their host galaxies are presented in the 3rd, 4th, 5th and 6th columns, respectively. The 7th column indicates the redshift z . D_{25} is given in column eight. The angle Θ expressed in arcsec is shown in the 9th column. Columns 10 and 11 contain the absolute distance D in kpc and relative separation normalized to the size of the host galaxies, respectively.

In Fig. 11 we present the relative separation between SNe and their host galaxies depending on the redshift. To evaluate how far supernova is we chose a value of 1 for the relative separation which is shown by the horizontal green line in Fig. 11. There are eight SNe IIb that lie above the solid green line, we collect them into a group of distant supernovae. SN 2017gpn is the most distant from the host galaxy center among the confirmed SNe IIb.

After that, we collected images for all these distant SNe with the goal to investigate their unexpected location (see Fig. 12). The majority of them are in continuations of spiral arms, e.g. supernovae 1997dd or 2001cf. Exceptions are supernovae 2011ft and 2017gpn, which are well outside the borders of their host galaxies. We found Pan-STARRS1 images (Chambers et al. 2016; Flewelling et al. 2016) for SN 2011ft in r , i , z and y passbands where one can notice a diffused red object exactly at the SN 2011ft position, which can be associated with the host galaxy of SN 2011ft.

Besides, we consider the object with the highest relative separation in Fig. 11 (Rel. Sep. is 2.67, see Table A1) — SN 2017ati — a candidate to Type IIb SNe. It turns out that this SN exploded in the system of interacting galaxies. Due to this interaction, a region with a high star formation rate could be formed, and this explains the detection of the core-collapse supernova far from the host galaxy disk. Therefore, SN 2017gpn is the only one distant SNe that is not located in the region with the high star formation rate.

According to the stellar evolution theory, the progenitor

star of SN IIb should be a massive star with the initial mass of $\sim 30 M_\odot$. The fact that SN 2017gpn exploded far from the region with the high star formation rate challenges this popular scenario. We have considered three different hypotheses to explain its location.

First, the progenitor of SN 2017gpn could be a super-speed star. Brown et al. (2005) have discovered a hyper-velocity star SDSS J090745.0+024507 with the mass of $\sim 4 M_\odot$ ejected from the Milky Way center and left with the velocity of 709 km s^{-1} . If we presume that the SN 2017gpn progenitor mass is about $30 M_\odot$, the average lifetime of such star will be ~ 3 million years calculated by formula $t_{\text{life}} \simeq \left(\frac{M_\odot}{M_{\text{star}}} \right)^2$. If it moves at the speed of 1000 km s^{-1} (Hills 1988), it could move away from the center of the host galaxy for ~ 29 kpc during its lifetime. However, such a high velocity implies that the kinetic energy is $\sim 3 \times 10^{50} \text{ erg}$, therefore an effective mechanism of the star acceleration is required.

The second hypothesis is that a part of the spiral arm of the host galaxy NGC 1343 is faint and therefore cannot be easily observed. For example, the similar situation is observed for the object AM 1316-241 (Keel & White 2001; see Fig. 13). In this case we can see the faint spiral arm of the galaxy only because it is illuminated by the light of a background elliptical galaxy. It is important that this part of the spiral structure does not lie on the continuation of the bright spiral arm; therefore, a SN explosion there (in the absence of a “lamp” behind) will look like being outside the galaxy.

The third hypothesis is that the host galaxy of SN 2017gpn experienced an interaction with other galaxies in the past. Tidal force destroyed the satellite galaxy and provided enough amount of gas which could condense far from the NGC 1343 center. Moreover, we can see the interaction between the galaxy ZOAG G134.74+13.65 and the SN 2017gpn host galaxy that also could cause the formation of gas clouds with the high star formation rate.

4.5 Connection with G299232

Initially SN 2017gpn was considered as a possible optical counterpart of the GW event G299232 since it was discovered 2 days later in its error box⁴. If we assume that the gravitational energy is released by the collapse, GW events are expected from supernova explosions (Herant et al. 1994) and could be detected by the LIGO/Virgo experiment (The LIGO Scientific Collaboration et al. 2019).

Nevertheless, the results of the hydrodynamic modelling show that explosion happened on Aug 20 (~ 3.5 days before GW alert) following the best-fit model, or on Aug 17 for the additional model, i.e. ~ 8 days before registration of G299232. G299232 is a low-significance event, therefore it could be a false signal, even if it is not, still it is implausible that SN 2017gpn can be associated with this alert. Both of our calculated models do not favor the electromagnetic counterpart of the gravitational event.

⁴ <https://gcn.gsfc.nasa.gov/other/G299232.gcn3>

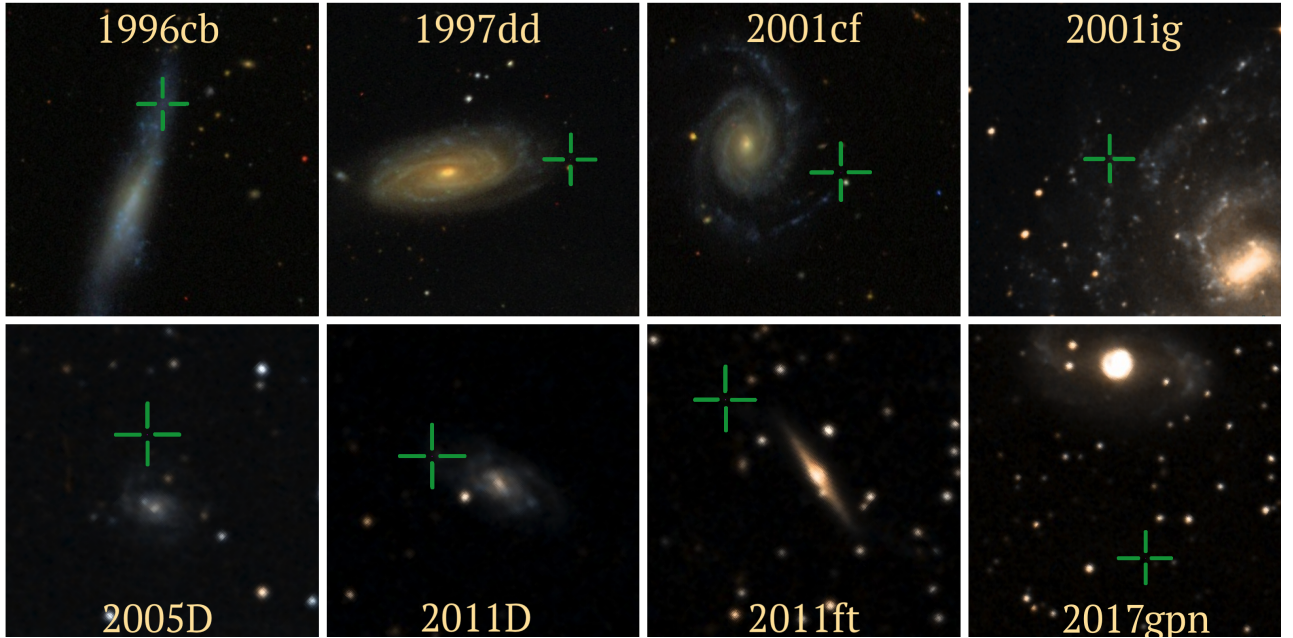


Figure 12. Optical images of supernovae distant from their host galaxies centers. SNe are marked by green crosses. All images were provided by SDSS([Blanton et al. 2017](#); [Gunn et al. 1998](#)) and DSS.

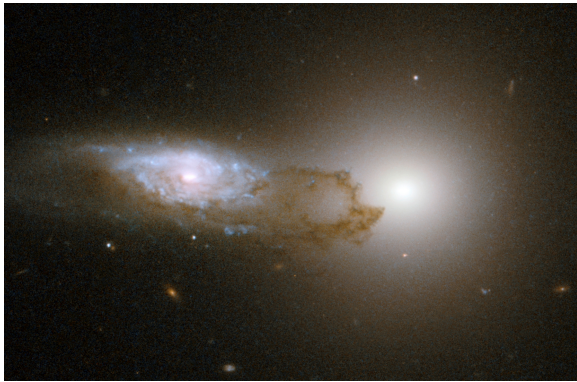


Figure 13. The image of AM 1316-241 obtained by the Hubble Space Telescope ([Keel & White 2001](#)). The faint spiral arms are visible owing to the light from the background elliptical galaxy.

5 CONCLUSIONS

In this paper we presented spectroscopic and photometric observations of the Type I Ib Supernova 2017gpn and the results of the numerical modelling of its B , R light curves with the STELLA code. The best-fit hydrodynamic model has the following values of parameters: the pre-SN radius is $50 R_{\odot}$, the pre-SN mass — $3.5 M_{\odot}$, the mass of synthesised nickel totally mixed in the envelope — $0.11 M_{\odot}$, the mass of the compact remnant — $1.41 M_{\odot}$ (i.e. neutron star as a remnant) and the energy of the explosion — 1.2×10^{51} erg. We also determined the range for these parameters by considering the dependence of the modelled light curves on each parameter while the others remain fixed. The obtained ranges are $3-4 M_{\odot}$ for the pre-SN mass, $20-70 R_{\odot}$ for the pre-SN radius, $0.09-0.13 M_{\odot}$ for the mass of ^{56}Ni , and, finally, $(1.05-1.60) \times 10^{51}$ erg for E_{exp} .

The study of Type I Ib Supernovae is an important part of the exploration of the Universe chemical composition. The nucleosynthesis yields of CCSNe including SNe I Ib are characterized by strong contributions to the so-called alpha elements O, Ne, Mg, Si, S, Ar, Ca, and Ti ([Thielemann et al. 2018](#)) and the heavy elements, namely Ni, Co and Fe.

According to the Open Supernova Catalog ([Guillochon et al. 2017](#)) only about a couple of dozen SNe I Ib has a detailed photometry that allows to perform a reliable hydrodynamic modelling. Some of these SNe are considered in this paper and compared with SN 2017gpn taking into account a physically motivated classification of stripped-envelope SNe proposed by [Prentice & Mazzali \(2017\)](#). In this classification SN 2017gpn belongs to the I Ib(I) group which is characterized by the strong hydrogen line profiles before maximum light, that weaken greatly over time, and $\text{H } \alpha$ P-Cygni profile dominated by the absorption component. The analysis of the hydrodynamic modelling results of different SNe I Ib shows that the mass of synthesised ^{56}Ni is in the range $0.05-0.15 M_{\odot}$.

The modelling results for SN 2017gpn are consistent with those for SNe I Ib considered, especially if we compare them with the modelling results for SN 2008ax which is of I Ib(I) group according to [Prentice & Mazzali \(2017\)](#). These results together with the observational data presented here contribute to the study of the Type I Ib SN phenomena increasing the sample of well-studied SNe I Ib.

Finally, we considered three different hypotheses which could explain SN 2017gpn distant location relative to its host galaxy:

- the progenitor of SN 2017gpn is a hyper-velocity star ejected by NGC 1343 with an average speed more than 1000 km s^{-1} ;
- the progenitor is exploded in a faint spiral arm of the host galaxy;

- the progenitor is formed in a region of interaction between the host galaxy and another galaxy in the past.

However, still there is a chance that SN 2017gpn progenitor was not a massive star exploded for some reason far from the regions of the high star formation rate. A similar idea was proposed for the Type Ibn Supernova PS1-12sk by Hosseinzadeh et al. (2019). This question is open and challenges modern star evolution models.

ACKNOWLEDGEMENTS

E.A.B. acknowledges support from Russian Science Foundation grant 18-72-00159 for studying question of distant position SN 2017gpn relative host galaxy center. S.I.B. and M.V.P. acknowledges support from Russian Science Foundation grant 18-12-00522 for the supernova modelling with STELLA code. The authors acknowledge the support from the Program of development of M.V. Lomonosov Moscow State University (Leading Scientific School “Physics of stars, relativistic objects and galaxies”). The authors are grateful to O.I. Spiridonova and the Zeiss-1000 staff for the help in observations. We thank K.L. Malanchev and M.Sh. Potashov for the helpful discussion. X.Wang is supported by the National Natural Science Foundation of China (NSFC grants 11325313, 11633002, and 11761141001), and the National Program on Key Research and Development Project (grant no. 2016YFA0400803). We acknowledge the support of the staff of the Xinglong 2.16-m telescope. This work was partially supported by the Open Project Program of the Key Laboratory of Optical Astronomy, National Astronomical Observatories, Chinese Academy of Sciences. This research has made use of NASA’s Astrophysics Data System Bibliographic Services and following PYTHON software packages: NUMPY (van der Walt et al. 2011), MATPLOTLIB (Hunter 2007), ASTROPY (Astropy Collaboration et al. 2013; Price-Whelan et al. 2018).

REFERENCES

- Anderson J. P., et al., 2014, *ApJ*, **786**, 67
 Arnett W. D., 1982, *ApJ*, **253**, 785
 Astropy Collaboration et al., 2013, *A&A*, **558**, A33
 Audcent-Ross F. M., Meurer G. R., Audcent J. R., Ryder S. D., Wong O. I., Phan J., Williamson A., Kim J. H., 2019, arXiv e-prints, p. arXiv:1911.09842
 Baklanov P. V., Blinnikov S. I., Pavlyuk N. N., 2005, *Astronomy Letters*, **31**, 429
 Barbon R., Benetti S., Cappellaro E., Patat F., Turatto M., Iijima T., 1995, *A&AS*, **110**, 513
 Bersten M. C., et al., 2012, *ApJ*, **757**, 31
 Bersten M. C., et al., 2018, *Nature*, **554**, 497
 Blanton M. R., et al., 2017, *AJ*, **154**, 28
 Blinnikov S. I., Bartunov O. S., 1993, *A&A*, **273**, 106
 Blinnikov S. I., Eastman R., Bartunov O. S., Popolitov V. A., Woosley S. E., 1998, *ApJ*, **496**, 454
 Blinnikov S. I., Röpke F. K., Sorokina E. I., Gieseler M., Reinecke M., Travaglio C., Hillebrandt W., Stritzinger M., 2006, *A&A*, **453**, 229
 Blondin S., Tonry J. L., 2007, *ApJ*, **666**, 1024
 Branch D., 1992, *ApJ*, **392**, 35
 Brown W. R., Geller M. J., Kenyon S. J., Kurtz M. J., 2005, *ApJ*, **622**, L33
 Bufano F., et al., 2014, *MNRAS*, **439**, 1807
 Caimmi M., 2017, Transient Name Server Discovery Report, **2017-973**, 1
 Chambers K. C., et al., 2016, arXiv e-prints,
 Chugai N. N., et al., 2004, *MNRAS*, **352**, 1213
 Clocchiatti A., Wheeler J. C., 1997, *ApJ*, **491**, 375
 Copperwheat C. M., et al., 2017, GRB Coordinates Network, **21755**, 1
 Dessart L., Hillier D. J., 2005, *A&A*, **439**, 671
 Dessart L., Hillier D. J., 2006, *A&A*, **447**, 691
 Ergon M., et al., 2015, *A&A*, **580**, A142
 Filippenko A. V., 1997, *ARA&A*, **35**, 309
 Filippenko A. V., Matheson T., Ho L. C., 1993, *ApJ*, **415**, L103
 Flewelling H. A., et al., 2016, arXiv e-prints,
 Folatelli G., et al., 2006, *ApJ*, **641**, 1039
 Folatelli G., Bersten M. C., Kuncarayakti H., Benvenuto O. G., Maeda K., Nomoto K., 2015, *ApJ*, **811**, 147
 Guillochon J., Parrent J., Kelley L. Z., Margutti R., 2017, *ApJ*, **835**, 64
 Gunn J. E., et al., 1998, *AJ*, **116**, 3040
 Hakobyan A. A., Adibekyan V. Z., Aramyan L. S., Petrosian A. R., Gomes J. M., Mamon G. A., Kunth D., Turatto M., 2012, VizieR Online Data Catalog, pp J/A+A/544/A81
 Hakobyan A. A., et al., 2016, VizieR Online Data Catalog, p. J/MNRAS/456/2848
 Herant M., Benz W., Hix W. R., Fryer C. L., Colgate S. A., 1994, *ApJ*, **435**, 339
 Hills J. G., 1988, *Nature*, **331**, 687
 Hoflich P., Langer N., Duschinger M., 1993, *A&A*, **275**, L29
 Holmes S., et al., 2011, *Publications of the Astronomical Society of the Pacific*, **123**, 1177
 Hosseinzadeh G., McCully C., Zabludoff A. I., Arcavi I., French K. D., Howell D. A., Berger E., Hiramatu D., 2019, *ApJ*, **871**, L9
 Hunter J. D., 2007, *Computing in Science and Engineering*, **9**, 90
 Imshennik V. S., Nadezhin D. K., 1983, Soviet Scientific Reviews, Section E: Astrophysics and Space Physics Reviews, **2**, 75
 Jonker P. G., Fraser M., Nissanke S., Fender R. P., Broderick J., Rowlinson A., Wijers R. A. M. J., Stappers B., 2017, GRB Coordinates Network, **21737**, 1
 Kasen D., Branch D., Baron E., Jeffery D., 2002, *ApJ*, **565**, 380
 Keel W. C., White R. E., 2001, *ApJ*, **121**, 1442
 Komarov V. V., Komarova V. N., Moskvitin A. S., Drabek S. V., Emelyanov E. V., Shergin V. S., 2020, *Astronomical Journal of Azerbaijan*, p. in press
 Kozyreva A., et al., 2017, *MNRAS*, **464**, 2854
 Kromer M., Sim S. A., 2009, *MNRAS*, **398**, 1809
 Kumar B., et al., 2013, *MNRAS*, **431**, 308
 Landolt A. U., 1992, *AJ*, **104**, 340
 Lipunov V., et al., 2010, *Advances in Astronomy*, **2010**, 349171
 Lipunov V. M., et al., 2017, GRB Coordinates Network, **21719**, 1
 Makarov D., Prugniel P., Terekhova N., Courtois H., Vauglin I., 2014, *A&A*, **570**, A13
 Modjaz M., et al., 2014, *AJ*, **147**, 99
 Morales-Garoffolo A., et al., 2015, *MNRAS*, **454**, 95
 Nadyozhin D. K., Razinkova T. L., 1986, Nauchnye Informatsii, **61**, 29
 Nicholl M., 2018, *Research Notes of the AAS*, **2**, 230
 Nomoto K., Suzuki T., Shigeyama T., Kumagai S., Yamaoka H., Saio H., 1993, *Nature*, **364**, 507
 Paxton B., et al., 2018, *ApJS*, **234**, 34
 Pessi P. J., et al., 2019, *MNRAS*, **488**, 4239
 Piro A. L., Muhleisen M., Arcavi I., Sand D. J., Tartaglia L., Valentini S., 2017, *ApJ*, **846**, 94
 Prentice S. J., Mazzali P. A., 2017, *MNRAS*, **469**, 2672
 Price-Whelan A. M., et al., 2018, *AJ*, **156**, 123
 Qiu Y., Li W., Qiao Q., Hu J., 1999, *AJ*, **117**, 736

- Richmond M. W., Treffers R. R., Filippenko A. V., Paik Y., 1996,
AJ, **112**, 732
- Roberts D., Kolb U., 2018, [2](#)
- Rui L., et al., 2017, The Astronomer's Telegram, [10681](#)
- Sanders N. E., et al., 2015, *The Astrophysical Journal*, 799, 208
- Schlafly E. F., Finkbeiner D. P., 2011, *ApJ*, **737**, 103
- Sim S. A., Kromer M., Röpke F. K., Sorokina E. I., Blinnikov S. I., Kasen D., Hillebrandt W., 2010, in Pogorelov N. V., Audit E., Zank G. P., eds, Astronomical Society of the Pacific Conference Series Vol. 429, Numerical Modeling of Space Plasma Flows, Astronum-2009. p. 148 ([arXiv:0911.1549](#))
- Sobolev V. V., 1960, Moving envelopes of stars
- Springob C. M., Haynes M. P., Giovanelli R., Kent B. R., 2005, *ApJS*, **160**, 149
- Stetson P. B., 1987, in Bulletin of the American Astronomical Society. p. 745
- Tauris T. M., Langer N., Moriya T. J., Podsiadlowski P., Yoon S.-C., Blinnikov S. I., 2013, *ApJ*, **778**, L23
- The LIGO Scientific Collaboration et al., 2019, arXiv e-prints, [p. arXiv:1908.03584](#)
- Thielemann F.-K., Isern J., Perego A., von Ballmoos P., 2018, *Space Sci. Rev.*, **214**, 62
- Tominaga N., Blinnikov S., Baklanov P., Morokuma T., Nomoto K., Suzuki T., 2009, *ApJ*, **705**, L10
- Tsang B. T. H., Goldberg J. A., Bildsten L., Kasen D., 2020, arXiv e-prints, [p. arXiv:2006.01832](#)
- Tsvetkov D. Y., Volkov I. M., Baklanov P., Blinnikov S., Tuchin O., 2009, *Peremennye Zvezdy*, 29
- Tsvetkov D. Y., Volkov I. M., Sorokina E., Blinnikov S., Pavlyuk N., Borisov G., 2012, *Peremennye Zvezdy*, 32
- Volnova A. A., et al., 2017, *MNRAS*, **467**, 3500
- Wang X., 2017, The Astronomer's Telegram, [10684](#), 1
- Woosley S. E., Eastman R. G., Weaver T. A., Pinto P. A., 1994, *ApJ*, **429**, 300
- Woosley S. E., Kasen D., Blinnikov S., Sorokina E., 2007, *ApJ*, **662**, 487
- Yoon S.-C., Dessart L., Clocchiatti A., 2017, *ApJ*, **840**, 10
- van der Walt S., Colbert S. C., Varoquaux G., 2011, *Computing in Science and Engineering*, **13**, 22

APPENDIX A: TABLE

Table A1: A complete list of confirmed Type Ib Supernovae and candidates to SNe Ib.

N ^o	SN name	R.A. _{SN}	Dec. _{SN}	R.A. _{Host}	Dec. _{Host}	<i>z</i>	D_{25} ["]	Θ ["]	D [kpc]	Rel. Sep.
1	SN1987K	12 43 41.17	+16 23 44.9	12 43 42.63	+16 23 36.2	0.0027	233.43	22.74	1.27	0.19
2	SN1993J	09 55 24.77	+69 01 13.7	09 55 33.17	+69 03 55.1	0.0008	1312.66	167.57	2.78	0.26
3	SN1996cb	11 03 41.98	+28 54 13.7	11 03 43.41	+28 53 13.9	0.0024	92.93	62.68	3.11	1.35
4	SN1997dd	16 05 46.33	+21 29 14.2	16 05 51.98	+21 29 05.9	0.0147	114.33	79.30	23.77	1.39
5	SN1998fa	06 42 51.51	+41 25 18.9	06 42 51.76	+41 25 14.9	0.0250	57.3	4.89	2.46	0.17
6	SN2000H	06 51 07.67	+12 55 18.5	06 51 06.28	+12 55 19.4	0.0130	101.89	20.34	5.40	0.40
7	SN2001cf	12 02 31.64	+41 02 58.9	12 02 36.56	+41 03 15.0	0.0200	68.89	57.94	23.48	1.68
8	SN2001gd	13 13 23.89	+36 38 17.7	13 13 27.54	+36 35 37.1	0.0029	586.34	166.50	9.99	0.57
9	SN2001g	22 57 30.69	-41 02 25.9	22 57 18.36	-41 04 14.5	0.0031	300.71	176.76	11.33	1.18
10	SN2001Q	11 25 19.77	+63 43 15.6	11 25 19.05	+63 43 45.4	0.0124	140.65	30.18	7.65	0.43
11	SN2002au	09 34 37.60	+05 50 15.7	09 34 38.62	+05 50 29.2	0.0180	65.79	20.34	7.44	0.62
12	SN2002eg	19 49 47.25	+50 41 53.6	19 49 48.75	+50 41 46.0	0.0260	53.48	16.15	8.45	0.60
13	SN2003bg	04 10 59.43	-31 24 50.4	04 11 00.65	-31 24 27.8	0.0046	101.89	27.47	2.61	0.54
14	SN2003cv	11 17 48.30	+19 09 08.5	11 17 48.37	+19 09 05.4	0.0288	16.53	3.25	1.88	0.39
15	SN2003ed	13 47 45.40	+38 18 21.1	13 47 44.99	+38 18 16.4	0.0045	52.26	6.74	0.63	0.26
16	SN2003gu	23 02 59.45	+34 43 19.6	23 02 59.10	+34 43 37.7	0.0190	60.00	18.61	7.17	0.62
17	SN2003ki	07 51 33.24	+63 55 51.6	07 51 34.20	+63 55 42.0	0.0250	46.57	11.50	5.79	0.49
18	SN2004be	10 00 19.47	-24 48 13.8	10 00 19.30	-24 48 08.0	0.0076	56.00	6.24	0.98	0.22
19	SN2004bi	10 47 37.45	+26 18 12.0	10 47 39.37	+26 17 41.5	0.0220	84.75	39.96	17.77	0.94
20	SN2004bm	10 52 35.33	+22 56 05.5	10 52 35.75	+22 56 02.8	0.0042	140.65	6.40	0.56	0.09
21	SN2004c	11 27 29.76	+56 52 48.4	11 27 31.89	+56 52 36.2	0.0057	104.27	21.30	2.50	0.41
22	SN2004ex	00 38 10.19	+02 43 17.2	00 38 12.38	+02 43 42.6	0.0180	111.73	41.50	15.17	0.74
23	SN2004ff	04 58 46.19	-21 34 12.0	04 58 47.12	-21 34 09.9	0.0230	73.82	13.14	6.10	0.36
24	SN2004gj	11 30 59.63	+20 28 06.8	11 31 00.66	+20 28 08.6	0.0210	44.48	14.59	6.20	0.66
25	SN2005D	07 26 57.36	+20 22 53.4	07 26 57.12	+20 22 15.5	0.0280	45.51	38.05	21.38	1.67
26	SN2005em	03 13 47.71	-00 14 37.0	03 13 47.69	-00 14 36.7	0.0252	95.09	0.42	0.22	0.01
27	SN2005H	02 09 38.52	-10 08 43.6	02 09 38.56	-10 08 46.1	0.0128	80.94	2.57	0.67	0.06
28	SN2005U	11 28 33.22	+58 33 42.5	11 28 31.33	+58 33 41.8	0.0010	143.93	14.80	0.31	0.21
29	SN2006ba	09 43 13.40	-09 36 53.0	09 43 11.98	-09 36 44.5	0.0190	106.70	22.66	8.73	0.42
30	SN2006bf	12 58 50.68	+09 39 30.1	12 58 50.91	+09 39 14.7	0.0240	57.30	15.77	7.63	0.55
31	SN2006el	22 47 38.50	+39 52 27.6	22 47 37.39	+39 52 44.8	0.0170	47.66	21.43	7.41	0.90
32	SN2006iv	11 48 12.35	+54 59 14.6	11 48 11.32	+54 59 30.2	0.0081	88.75	17.94	2.99	0.40
33	SN2006qp	14 42 30.65	+28 43 25.9	14 42 33.24	+28 43 35.2	0.0120	119.72	35.32	8.67	0.59
34	SN2006T	09 54 30.21	-25 42 29.3	09 54 28.64	-25 42 11.8	0.0081	212.89	27.50	4.58	0.26
35	SN2007ay	08 17 14.85	+01 12 06.9	08 17 15.73	+01 12 23.0	0.0150	45.51	20.82	6.37	0.91
36	SN2008aq	12 50 30.42	-10 52 01.4	12 50 29.39	-10 51 15.7	0.0080	198.68	48.15	7.92	0.48
37	SN2008ax	12 30 40.80	+41 38 14.5	12 30 36.41	+41 38 37.4	0.0019	405.65	54.28	2.14	0.27
38	SN2008ay	12 55 26.36	+52 16 15.5	12 55 24.90	+52 16 03.5	0.0344	68.89	17.99	12.32	0.52
39	SN2008bo	18 19 54.34	+74 34 20.9	18 19 46.42	+74 34 06.2	0.0049	198.68	34.86	3.53	0.35
40	SN2008cx	00 56 45.90	-09 54 19.0	00 56 42.66	-09 54 50.1	0.0189	134.32	57.09	21.89	0.85
41	SN2008ie	02 43 20.80	+04 58 19.1	02 43 22.27	+04 58 06.2	0.0137	140.65	25.47	7.13	0.36
42	SN2009C	23 13 42.84	+49 40 47.2	23 13 43.95	+49 40 35.7	0.0236	49.91	15.76	7.50	0.63

43	SN2009gk	21 44 27.28	+14 53 57.3	21 44 28.76	+14 53 59.2	0.0264	58.63	21.54	11.43	0.73
44	SN2009jv	09 40 57.83	+47 37 04.0	09 40 58.19	+47 37 13.3	0.0161	90.81	9.99	3.27	0.22
45	SN2009K	04 36 36.77	-00 08 35.6	04 36 37.35	-00 08 37.0	0.0117	208.04	8.81	2.11	0.08
46	SN2009mk	00 06 21.37	-41 28 59.8	00 06 19.92	-41 29 59.6	0.0051	150.71	61.98	6.52	0.82
47	SN2010am	09 33 01.75	+15 49 08.8	09 33 02.11	+15 49 16.1	0.0200	27.20 ⁺	8.96	3.63	0.65
48	SN2010cn	11 04 06.57	+04 49 58.7	11 04 06.40	+04 49 55.5	0.0260	30.30 ⁺	4.09	2.14	0.27
49	SN2010ei	14 54 07.69	+42 32 54.6	14 54 07.71	+42 32 53.2	0.0187	20.20 ⁺	1.42	0.54	0.14
50	SN2010ej	14 13 56.74	+31 32 25.1	14 13 56.56	+31 32 24.7	0.0523	12.54	2.34	2.38	0.37
51	SN2010ek	22 48 40.96	+27 37 11.4	22 48 40.80	+27 36 40.0	0.0320	70.49	31.47	20.12	0.89
52	SN2011bp	11 12 29.96	+31 23 05.5	11 12 30.16	+31 23 05.9	0.0275	23.89	2.59	1.43	0.22
53	SN2011D	03 02 14.53	+17 20 58.3	03 02 12.23	+17 20 43.7	0.0231	43.47	36.02	16.80	1.66
54	SN2011dh	13 30 05.11	+47 10 10.9	13 29 52.70	+47 11 43.0	0.0016	828.23	156.49	5.19	0.38
55	SN2011ft	17 52 42.98	+29 04 10.6	17 52 39.46	+29 03 32.4	0.0173	62.83	59.91	21.07	1.91
56	SN2011fu	02 08 21.40	+41 29 12.3	02 08 21.49	+41 28 45.1	0.0190	90.81	27.22	10.49	0.60
57	SN2011hs	22 57 11.77	-43 23 04.8	22 57 13.57	-43 23 46.1	0.0057	337.40	45.72	5.37	0.27
58	SN2012P	14 59 59.04	+01 53 24.4	15 00 00.43	+01 53 28.6	0.0045	181.20	21.26	1.98	0.23
59	SN2013ak	08 07 06.69	-28 03 10.1	08 07 08.00	-28 03 08.0	0.0037	140.65	17.47	1.34	0.25
60	SN2013bb	14 12 13.96	+15 50 31.5	14 12 15.81	+15 50 30.9	0.0175	70.49	26.70	9.50	0.76
61	SN2013df	12 26 29.33	+31 13 38.3	12 26 27.09	+31 13 24.8	0.0024	116.99	31.75	1.58	0.54
62	SN2014ds	08 11 16.45	+25 10 47.4	08 11 15.92	+25 10 45.7	0.0137	44.48	7.39	2.07	0.33
63	SN2015bi	14 32 15.31	+26 19 32.0	14 32 15.19	+26 19 36.2	0.0160	42.48	4.50	1.47	0.21
64	SN2016adj	13 25 24.12	-43 00 57.9	13 25 27.60	-43 01 08.8	0.0018	1542.24	39.69	1.48	0.05
65	SN2016gkg	01 34 14.46	-29 26 25.0	01 34 18.24	-29 25 06.6	0.0049	322.22	92.66	9.37	0.58
66	SN2017gpn	03 37 44.97	+72 31 59.0	03 37 49.72	+72 34 16.6	0.0074	143.93	139.25	21.20	1.93
67	ASASSN-14az	23 44 48.00	-02 07 03.2	23 44 48.27	-02 06 53.4	0.0067	38.74	10.6	1.46	0.55
68	ASASSN-14dq	21 57 59.97	+24 16 08.1	21 57 59.82	+24 15 59.7	0.0104	79.10	8.65	1.84	0.22
69	ASASSN-15bd	15 54 38.33	+16 36 38.1	15 54 38.39	+16 36 37.6	0.0080	22.81	1.00	0.16	0.09
70	PS15cj	02 38 07.29	+01 23 29.2	02 38 07.57	+01 23 18.1	0.0229	72.14	11.87	5.49	0.33
71	PTF11iqb	00 34 04.84	-09 42 17.9	00 34 02.79	-09 42 19.0	0.0125	157.82	30.33	7.75	0.38
72	SN2001ad*	17 24 02.40	+58 59 52.0	17 24 08.11	+58 59 42.4	0.0110	61.40	45.15	10.17	1.47
73	SN2002hz*	22 27 49.54	+38 35 09.5	22 27 48.30	+38 35 11.7	0.0180	99.58	14.70	5.38	0.30
74	SN2002jz*	04 13 12.52	+13 25 07.3	04 13 12.40	+13 25 19.1	0.0052	60.00	11.93	1.28	0.40
75	SN2005by*	13 45 46.91	+22 05 46.8	13 45 45.62	+22 05 18.4	0.0270	75.54	33.59	18.22	0.89
76	SN2005lr*	07 11 39.03	-26 42 20.2	07 11 40.45	-26 42 17.9	0.0086	125.36	19.17	3.39	0.31
77	SN2006ss*	14 20 27.46	+35 11 42.7	14 20 26.50	+35 11 19.1	0.0120	88.75	26.37	6.48	0.59
78	SN2008cw*	16 32 38.27	+41 27 33.2	16 32 38.00	+41 27 33.0	0.0320	25.59	3.04	1.94	0.24
79	SN2008gx*	10 15 32.95	+74 12 59.1	10 15 32.22	+74 13 13.1	0.0215	67.32	14.31	6.22	0.43
80	SN2009ej*	00 30 28.56	-33 12 56.0	00 30 21.89	-33 14 43.3	0.0053	499.06	136.08	14.88	0.55
81	SN2009mg*	06 21 44.86	-59 44 26.0	06 21 38.91	-59 44 24.0	0.0076	143.93	45.02	7.04	0.63
82	SN2009Z*	14 01 53.61	-01 20 30.2	14 01 53.80	-01 20 35.6					
83	SN2010ir*	05 19 35.80	-32 39 28.2	05 19 35.81	-32 39 27.9	0.0124	82.82	0.33	0.08	0.01
84	SN2011bv*	13 02 53.57	-04 02 36.0							
85	SN2011cb*	22 47 07.49	-64 49 43.4	22 47 06.26	-64 49 55.4	0.0079	261.91	14.34	2.33	0.11
86	SN2011ef*	23 30 57.02	+15 29 24.3	23 30 56.80	+15 29 26.0	0.0134	64.29	3.61	0.99	0.11
87	SN2011ei*	20 34 22.62	-31 58 23.6	20 34 21.00	-31 58 51.0	0.0093	280.64	34.29	6.55	0.24
88	SN2011hg*	23 11 48.84	+31 01 00.4	23 11 50.29	+31 01 16.2	0.0236	92.93	24.44	11.64	

89	SN2012cd*	13 22 35.25	+54 48 47.0	13 22 32.43	+54 49 05.0	0.0118	51.07	30.30	7.32	1.19
90	SN2012dy*	21 18 50.70	-57 38 42.5	21 18 50.99	-57 38 25.2	0.0103	128.28	17.46	3.69	0.27
91	SN2012fg*	09 24 37.95	+49 21 32.0	09 24 37.73	+49 21 25.5	0.0163	114.33	6.85	2.27	0.12
92	SN2012hb*	09 02 05.46	-64 54 19.7	09 02 05.52	-64 54 16.2	0.0056	80.94	3.52	0.41	0.09
93	SN2012hs*	09 49 14.71	-47 54 45.6	09 49 16.53	-47 55 12.9	0.0064	111.73	32.86	4.33	0.59
94	SN2013bl*	08 46 15.06	+41 34 40.0	08 46 14.07	+41 34 47.5	0.0304	62.83	13.40	8.15	0.43
95	SN2013cu*	14 33 58.97	+40 14 20.7	14 33 59.00	+40 14 40.0	0.0252	67.32	19.30	9.80	0.57
96	SN2013ep*	22 58 30.35	+40 25 44.5	22 58 29.31	+40 25 46.3					
97	SN2013fq*	19 59 07.95	-55 55 46.6	19 59 06.40	-55 55 41.6					
98	SN2014cq*	09 23 29.55	-63 40 28.3	09 23 26.79	-63 40 45.3	0.0110	109.18	25.02	5.64	0.46
99	SN2014ds*	08 11 16.45	+25 10 47.4	8 11 15.92	+25 10 45.7	0.0137	44.48	7.39	2.07	0.33
100	SN2015au*	22 30 59.42	-13 59 56.1	22 30 59.91	-14 00 12.8	0.0160	122.50	18.16	5.92	0.30
101	SN2015Y*	09 02 37.87	+25 56 04.2	09 02 38.64	+25 56 04.5	0.0080	84.75	10.39	1.71	0.25
102	SN2016avh*	10 25 47.80	-11 25 17.6	10 25 48.97	-11 25 28.5	0.0380	43.47	20.36	15.35	0.94
103	SN2016bas*	07 38 05.53	-55 11 47.0	07 38 05.53	-55 11 26.7	0.0090	128.28	20.30	3.75	0.32
104	SN2016bhr*	14 25 20.58	+32 28 55.9	14 25 20.59	+32 28 56.5	0.0139	32.97	0.61	0.17	0.04
105	SN2016blq*	11 08 55.51	-29 01 26.4	11 08 55.52	-29 01 25.5					
106	SN2016blt*	14 15 45.76	-47 38 15.0	14 15 45.64	-47 38 27.7	0.0160	79.10	12.76	4.16	0.32
107	SN2016bnd*	07 20 24.3	+32 51 01.2	07 20 24.60	+32 50 58.8					
108	SN2016dsb*	01 58 59.71	-32 22 18.5	01 59 00.57	-32 22 25.2					
109	SN2016exv*	03 39 34.38	+20 42 30.4	03 39 34.78	+20 42 31.9	0.0212	36.15	5.81	2.49	0.32
110	SN2016hkn*	02 08 34.23	+29 14 11.1	02 08 34.37	+29 14 02.6	0.0219	36.15	8.70	3.85	0.48
111	SN2016iyc*	22 09 14.20	+21 31 17.5	22 09 15.30	+21 31 06.8	0.0127	49.91	18.71	4.86	0.75
112	SN2016ye*	07 45 19.72	-71 24 17.9	07 45 15.96	-71 24 37.6	0.0180	90.81	26.67	9.75	0.59
113	SN2016M*	07 16 37.75	+67 53 32.3	07 16 36.07	+67 53 42.2	0.0360	27.43	13.71	9.81	1.00
114	SN2016U*	10 34 19.27	+03 24 25.5	10 34 19.10	+03 24 22.9	0.0740	21.78	3.64	5.12	0.33
115	SN2017ati*	09 49 56.70	+67 10 59.6	09 49 50.40	+67 11 11.0	0.0131	28.72	38.38	10.27	2.67
116	SN2017cao*	19 24 02.19	+42 17 21.1	19 24 02.15	+42 17 27.6	0.0200	23.34	6.52	2.64	0.56
117	SN2017dgd*	16 45 38.967	+01 37 19.7	16 45 39.02	+01 37 13.1					
118	SN2017eiy*	23 49 28.27	-30 25 04.7	23 49 28.64	-30 25 14.8	0.0470	45.51	11.18	10.31	0.49
119	SN2017fek*	20 21 47.44	-10 43 53.3	20 21 47.70	-10 43 46.0	0.0330	49.91	8.24	5.43	0.33
120	SN2017gfh*	20 03 27.40	+06 59 27.2	20 03 27.78	+06 59 22.8	0.0245	51.07	7.17	3.54	0.28
121	SN2017gfz*	00 12 51.89	-32 43 53.0	00 12 51.80	-32 44 02.0	0.0600	18.54	9.07	10.52	0.98
122	SN2017gkk*	09 13 44.37	+76 28 42.4	09 13 43.04	+76 28 31.2	0.0049	154.22	12.13	1.23	0.16
123	SN2017gth*	01 12 38.19	+05 45 58.4	01 12 38.20	+05 45 56.0	0.0380	28.72	2.40	1.81	0.17
124	SN2017hyh*	07 10 41.07	+06 27 41.4	07 10 40.48	+06 27 13.0	0.0120	39.64	29.73	7.30	1.50
125	SN2017jxz*	07 47 03.03	+26 46 25.8	07 47 02.32	+26 46 34.7	0.0240	27.43	13.02	6.30	0.95
126	SN2017jyd*	11 46 25.00	+01 59 33.1	11 46 24.70	+01 59 39.6	0.0285	19.42	7.90	4.52	0.81
127	SN2017jbl*	03 33 12.73	+36 11 24.6	03 33 13.19	+36 11 03.8	0.0151	49.91	21.53	6.63	0.86
128	SN2017jdn*	10 23 45.51	+53 06 20.5	10 23 46.90	+53 06 28.0	0.0317	45.51	14.59	9.24	0.64
129	SN2017jjo*	09 57 36.150	-22 10 23.91	09 57 36.41	-22 10 30.7					
130	SN2017mw*	09 57 20.97	-41 35 21.0	09 57 20.90	-41 35 28.0	0.0117	57.30	7.04	1.69	0.25
131	SN2018arx*	14 06 34.81	-32 34 44.1	14 06 35.05	-32 34 37.6	0.0339	58.63	7.17	4.85	0.24
132	SN2018bsg*	10 10 28.16	+02 13 48.8	10 10 27.86	+02 13 41.6	0.0217	58.63	8.49	3.73	0.29
133	SN2018ddr*	13 58 38.47	+07 13 01.2	13 58 38.56	+07 12 59.4	0.0146	82.82	2.24	0.67	0.05
134	SN2018dfg*	14 06 34.70	-05 27 02.9	14 06 34.89	-05 27 10.7	0.0095	137.45	8.30	1.62	

135	SN2018fcx*	04 05 56.72	-15 08 43.6	04 05 55.90	-15 08 58.9	0.0250	46.57	19.37	9.75	0.83
136	SN2018fex*	03 55 20.77	-56 45 14.6	03 55 21.66	-56 44 46.6	0.0243	37.86	28.94	14.18	1.53
137	SN2018fpb*	23 59 42.80	+34 20 39.9	23 59 42.96	+34 20 42.6	0.0148	32.22	3.35	1.01	0.21
138	SN2018gj*	16 32 02.31	+78 12 40.9	16 32 39.20	+78 11 53.5	0.0046	134.32	122.64	11.65	1.83
139	SN2018lhs*	23 49 58.18	+07 04 23.7	23 49 58.17	+07 04 19.7					
140	SN2018hqu*	12 16 33.78	+41 31 56.5	12 16 33.76	+41 31 56.0	0.0500	28.72	0.55	0.54	0.04
141	SN2018hyw*	08 20 17.38	+20 52 32.2	08 20 16.57	+20 52 30.3	0.0168	42.48	11.51	3.93	0.54
142	SN2018iuq*	07 05 53.44	+12 53 34.7	07 05 53.41	+12 53 36.8					
143	SN2018jak*	09 59 18.19	+34 53 43.8	09 59 18.13	+34 53 53.3	0.0385	38.74	9.53	7.27	0.49
144	SN2018jee*	07 23 14.632	+56 31 30.45	07 23 14.45	+56 31 29.6					
145	SN2018mc*	18 01 00.832	+61 41 46.92							
146	SN2018ow*	02 51 04.410	+09 06 44.32	02 51 04.80	+09 06 64.3					
147	SN2019abp*	16 23 26.53	+22 29 10.1	16 23 26.24	+22 29 08.6	0.0376				
148	SN2019abp*	16 23 26.534	+22 29 10.11	16 23 26.21	+22 29 08.6					
149	SN2019abp*	16 23 26.534	+22 29 10.11	16 23 26.21	+22 29 08.6					
150	SN2019ail*	10 28 27.28	+12 42 21.8	10 28 27.32	+12 42 14.6	0.0323	68.89	7.22	4.66	0.21
151	SN2019aur*	03 01 10.42	+41 23 45.8	03 01 10.15	+41 23 46.7	0.0124	43.47	3.17	0.80	0.15
152	SN2019bao*	10 29 18.52	+06 07 21.8	10 29 15.50	+06 07 40.8	0.0119	109.18	48.88	11.90	0.90
153	SN2019bzo*	15 55 34.45	+26 54 54.8	15 55 34.46	+26 54 54.0	0.0650				
154	SN2019daf*	13 47 48.12	+72 03 00.4	13 47 48.56	+72 02 59.8	0.0350	33.74	2.12	1.48	0.13
155	SN2019eev*	09 57 05.86	+08 04 10.17	09 57 05.86	+08 04 10.17					
156	SN2019eff*	16 33 39.14	+13 54 36.6	16 33 39.23	+13 54 23.6	0.0500	15.42	13.07	12.77	1.69
157	SN2019fco*	10 32 04.72	+46 55 03.6	10 32 04.34	+46 55 03.8	0.0406	20.33	3.90	3.13	0.38
158	SN2019fks*	21 41 16.50	-16 53 23.0	21 41 16.80	-16 53 23.0	0.0500	18.12	4.31	4.21	0.48
159	SN2019gal*	20 36 55.23	+02 48 24.6	20 36 54.90	+02 48 14.0	0.0060	31.49	11.70	1.45	0.74
160	SN2019ijj*	14 56 33.53	-25 50 10.9	14 56 33.62	-25 50 06.9	0.0290	33.74	4.18	2.43	0.25
161	SN2019fco*	16 18 38.54	+21 58 22.9	16 18 38.53	+21 58 24.0	0.0161	35.33	1.11	0.36	0.06
162	SN2019rn*	02 17 59.61	+14 32 00.4	02 17 59.65	+14 32 38.2	0.0131	114.33	37.80	10.12	0.66
163	SN2019xt*	14 11 55.741	-00 50 11.77	14 11 55.78	-00 50 12.0					
164	SNhunt268*	01 14 26.82	+42 33 18.4	01 14 26.27	+42 33 22.6	0.0197	77.29	7.39	2.95	0.19
165	ASASSN-15qz*	01 25 36.09	-41 27 55.8	01 25 35.80	-41 27 55.5	0.0216	36.15	3.27	1.43	0.18
166	CS151130 ¹ *	01 42 58.44	+27 34 10.5	01 42 57.60	+27 34 53.0					
167	DESI6S1kt*	02 51 07.54	+00 01 33.0	02 51 07.77	+00 01 30.8	0.0675	13.75	4.09	5.29	0.60
168	iPTF13efs*	07 55 26.19	+52 48 17.9	07 55 25.98	+52 48 24.7	0.0408	29.39	7.06	5.69	0.48
169	LSQ12hbo*	10 56 16.00	-20 51 32.0	10 56 12.97	-20 51 10.1	0.0122	79.10	47.79	11.93	1.21
170	LSQ12htu*	10 11 37.11	-07 23 11.6	10 11 37.68	-07 23 15.2	0.0520	21.29	9.21	9.34	0.87
171	LSQ13bca*	21 16 16.39	-20 30 48.9	21 16 16.80	-20 30 54.0	0.0800	25.01	7.69	11.62	0.62
172	LSQ14hj*	13 25 08.05	-32 37 32.8	13 25 07.90	-32 37 31.0	0.0500	22.81	2.61	2.55	0.23
173	LSQ15rw*	14 32 31.33	-13 39 27.4	14 32 31.19	-13 39 26.0	0.0210	43.47	2.47	1.05	0.11
174	OGLE16ekf*	04 37 36.66	-71 48 17.4	03 21 06.08	-07 16 56.8	0.0200	19.87	2.31	0.94	0.23
175	PS1-14od*	03 21 06.23	-07 16 57.4	03 21 06.08	-07 16 56.8					
176	PS15apj*	18 28 58.24	+22 54 10.6	18 28 57.36	+22 54 11.0	0.0140	56.00	12.17	3.48	0.43
177	PS15bgt*	22 46 05.04	-10 59 48.4	22 46 03.70	-11 00 04.3	0.0089	125.36	25.34	4.63	0.40
178	PS15bqc*	17 04 32.29	+01 20 58.5	17 04 32.26	+01 20 47.7	0.0230	37.00	10.81	5.02	0.58
179	PTF10htz*	13 08 37.52	+79 47 13.2	13 08 37.55	+79 47 13.3	0.0352	28.06	0.13	0.09	0.01

⁺ The value of D25 is measured as isophotal level of 25 mag arcsec⁻² in the SDSS g-band (Hakobyan et al. 2012, 2016).

^{*} Candidates to Type I Ib Supernovae.

1 CSS151130:014258+273410

This paper has been typeset from a T_EX/L_AT_EX file prepared by the author.